Biomass Conversion and Biorefinery
https://doi.org/10.1007/s13399-023-04337-z

ORIGINAL ARTICLE

Synthesis of Ag nanoparticles loaded with potassium polyacrylate hydrogel for rose bengal dye removal and antibacterial activity

Abdelhakim Boutalbi[1,2] · Souhaila Meneceur[1,2] · Salah Eddine Laouini[1,2] · Hamdi Ali Mohammed Mohammed[1,2] · Gamil Gamal Hasan[1,2] · Abderrhmane Bouafia[1,2]

Received: 20 March 2023 / Revised: 5 May 2023 / Accepted: 11 May 2023

Abstract

Silver nanoparticles have recently gained significant attention due to their remarkable properties as photocatalysts and antimicrobial agents. However, their widespread use has been hampered by several issues such as aggregation and stabilization. To address these challenges, this study explores the incorporation of silver nanoparticles within potassium polyacrylate (PPA) hydrogel. The integration process was accomplished through in-situ reduction of silver ions using sodium borohydride. The synthesized PPA/Ag nanocomposite was characterized by using UV–visible, XRD, SEM, and FTIR techniques. The silver nitrate ($AgNO_3$) sample had an indirect optical bandgap of 3.3 eV, but adding PPA decreased it to 2.42 eV. The prepared PPA/Ag composites exhibited superior photocatalytic activity in the degradation of rose bengal dye. The highest degradation efficiency of 95% was observed for PPA/Ag (16 mM), while the lowest efficiency of 88% was recorded for PPA/Ag (10 mM). To assess the antibacterial effectiveness of the four PPA/Ag samples (2 mM, 5 mM, 10 mM, and 16 mM) against various bacteria such as *E. coli*, *P. aeruginosa*, and *S. aureus*, the agar diffusion technique was employed. The results show that the largest inhibition zones were achieved in the presence of PPA/Ag (2 mM) samples against *E. coli* and *P. aeruginosa* bacterial strains, while PPA/Ag (10 mM) presented a better effect against *S. aureus* than the other prepared samples. Additionally, the prepared samples demonstrated excellent antimicrobial properties against diverse microorganisms. This finding makes PPA/Ag potentially useful in applications such as wastewater treatment and wound healing.

Keywords Silver nanoparticles · Potassium polyacrylate hydrogel · Photocatalytic · Antimicrobial · Synthesis

1 Introduction

The world has witnessed a dramatic increase in population and massive industrial activities in the last decades, leading to injurious chemical substances taking over as the primary contributor to water pollution. For instance, organic dyes are frequently released into the local environment along with wastewater without being sufficiently treated. The rapid and practical removal of organic dyes from wastewater has been a challenging problem for scientists to solve [1–3] because of their unique properties, including catalytic, optical, and magnetic properties [4, 5]. Metal and metallic nanoparticles have been studied in a variety of scientific fields, such as energy science, agriculture, textiles, and the environment.

These metallic nanoparticles, in particular, have been used successfully for water splitting and wastewater management as catalysts [6] and for a variety of chemical redox reactions (e.g., the mineralization of natural contaminations in wastewater) [7]. Because of their broad-spectrum

✉ Abderrhmane Bouafia
abdelrahmanebouafia@gmail.com

Abdelhakim Boutalbi
a.hakimbout@gmail.com

Souhaila Meneceur
menaceursouheila@yahoo.fr

Salah Eddine Laouini
salah_laouini@yahoo.fr

Hamdi Ali Mohammed Mohammed
hamdimohammed116@gmail.com

Gamil Gamal Hasan
hasan_gamil@yahoo.com

[1] Department of Process Engineering and Petrochemical, Faculty of Technology, University of El Oued, 39000 El Oued, Algeria

[2] Laboratory of Biotechnology Biomaterials and Condensed Matter, Faculty of Technology, University of El Oued, 39000 El Oued, Algeria

Published online: 17 May 2023

antimicrobial activity [8, 9], ease of accessibility, and low drug resistance, metallic nanoparticles have also been used as antimicrobial and anticancer agents in biomedical applications [10, 11].

Rose bengal is a synthetic dye that is commonly used in textile, printing, and paper industries and is known to be persistent in the environment, causing potential health and environmental hazards. The degradation of rose bengal dye can be challenging due to its complex structure and resistance to conventional degradation methods [12]. However, AgNPs-based hydrogel has shown promising results in degrading rose bengal dye. The hydrogel matrix provides a stable and porous structure that allows for the effective dispersion and immobilization of AgNPs, enhancing their catalytic activity. Moreover, the hydrogel matrix can act as a barrier, preventing the release of AgNPs into the environment [13].

Among different metallic nanoparticles, silver nanoparticles have gained significant attention in the past decades. However, some issues may prevent their use, such as the fact that silver nanoparticles smaller than 50 nm in free form can be toxic to human health and the environment. Also, silver nanoparticles have a high active surface area, which gives them a natural tendency to aggregate in solution over time [14, 15]. Additionally, the separation process of metallic nanoparticles from the solutions is still one of the most favorable requirements [16]. A further issue that can adversely affect the use of metallic nanoparticles is that they are not stabilized materials. The above-mentioned issues can be easily overcome by the incorporation of silver nanoparticles in or with hydrogels. Hydrogels are three-dimensional networks; they have the ability to swell and absorb water or aqueous solutions (without dissolving in them) hundreds of times their dry weight within their structure. Hydrogels have outstanding characteristics such as hydrophilicity, high swelling ratio, stimulus response, and biocompatibility [17], allowing them to be used successfully in agriculture, biomedical, pharmaceuticals, biosensors, drug delivery, tissue engineering, and separation devices [18–23].

In their swollen form, hydrogels provide suitable support for nanoparticles intended for use in aqueous-based reactions [24, 25]; they can provide free space between networks that serve as nanoreactors and serve for nanoparticle nucleation and growth. Moreover, the available free-network spaces between hydrogel networks allow the formation and stabilization of the nanoparticles within. Therefore numerous hydrogels based on natural polymers like chitosan, gelatin, and starch or synthetic polymers like polysaccharide, poly(acrylamide) N-isopropylacrylamide, and sodium acrylate [26–31] were loaded with metallic nanoparticles for the purposes of photocatalysis and antimicrobial activity. The practical incorporation of nanotechnology in pharmaceuticals has led to research on the antimicrobial properties of inorganic nanoparticles (NPs), such as metals (Ag, Au, Cu, and Pt) and metal oxides (Ag_2O, TiO_2, SiO_2, CuO, ZnO, CaO, MgO, and Fe_2O_3) [13, 32, 33]. Among these, Ag NPs have been extensively studied and utilized in various biomedical applications due to their efficacy as antibacterial, antifungal, antiviral, and anti-inflammatory agents. Specifically, Ag NPs have been found to strongly adsorb onto microorganisms and disrupt their biochemical pathways through various mechanisms, such as the generation of reactive oxygen species (ROS) and the inhibition of electron transfer reactions [34, 35].

As supports for the fabrication of AgNPs, a variety of hydrogels including chitosan, alginate, collagen, and gelatin have been employed. Due to its outstanding biocompatibility, biodegradability, and simplicity of functionalization, chitosan is the hydrogel that is used the most frequently among these. For instance, AgNPs for the treatment of bacterial infections have been created using chitosan hydrogels. In a study by Pengrui Jin et al. (2022) [36], AgNPs were created using chitosan hydrogels and then put onto polyurethane foam to treat wound infections.

These experiments show the possibility of employing hydrogels as manufacturing substrates for silver nanoparticles with significant antibacterial properties. Further study is required to improve the synthesis procedure and assess these materials' performance in various applications because the hydrogel choice can have an impact on the properties of the final product.

Earlier investigations have explored the potential of utilizing cross-linked potassium acrylate polymer as a constituent of water-absorbing geocomposites for the purpose of sequestering soil water and conveying it to the interior of a spatially arranged skeletal structure [37, 38]. The present study sought to enhance the performance of the hydrogel by incorporating Ag NPs and to evaluate its effectiveness as a novel composite material for the degradation of dyes in wastewater and for exhibiting antibacterial properties.

In this study, by encapsulating silver nanoparticles with potassium polyacrylate hydrogel (PPA/Ag) as a suitable substrate for stabilization of silver nanoparticles and also by using the high porosity of potassium polyacrylate, stable nanoparticles with high porosity and contact surface were synthesized. Silver nanoparticles have good antibacterial properties, and also, the porosity of PPA improves the photocatalytic properties of Ag NPs. In this research, the design, fabrication, and characterization of PPA hydrogel are functionalized with mesoporous Ag nanoparticles for use as novel agents for antibacterial photocatalytic activities. As far as we know, this is the initial documentation of the production of PPA/Ag nanocomposites. PPA/Ag nanocomposite was characterized by XRD, FTIR, SEM, and UV–Vis. The obtained Ag-Gels nanocomposites were used for the photodegradation of rose bengal dye as photocatalysis under sunlight irradiation to evaluate the photocatalytic performance, and they were also tested against different bacterial strains as antimicrobial materials to evaluate the antimicrobial performance as well.

2 Materials and methods

2.1 Materials

Potassium polyacrylate hydrogel was purchased from ARTAGR O POLSKA, Poland. Silver nitrate ($AgNO_3$ 99.92%), sodium borohydride ($NaBH_4$ 98%), and rose bengal were purchased from Biochem Chemophara, United Kingdom. Mueller Hinton agar was purchased from Biokar diagnostics, France. Nutrient agar was purchased from Titan Biotech LTD, India, and Double distilled water was used for preparing solutions.

2.2 Preparation of Ag NPs loaded with potassium polyacrylate hydrogel

The preparation of silver nitrate nanoparticles (Ag NPs) within potassium polyacrylate (PPA) hydrogel was achieved through a facile method which was reported in the literature [29, 30]. First, a stock solution of silver nitrate was prepared, and then the dry PPA hydrogel that had been precisely weighed was immersed in the silver nitrate solution in beakers containing 30 ml of different concentrations (2 mM, 5 mM, 10 mM, and 16 mM) for 24 h to get silver ions-loaded gels. At this point, the silver ions were transferred from the solution into the hydrogel structure by filling free spaces in the hydrogel networks and by anchoring through the presence of hydrogel chemical groups such as hydroxylic (-OH), carboxylic (-COOH), amidic (-CONH-), and primary amidic ($-CONH_2$). Next, a stock solution of sodium borohydride was prepared, and the swollen hydrogel loaded with Ag^+ ions was taken out and immersed in the sodium borohydride solution in beakers containing 30 ml of different concentrations (4 mM, 10 mM, 20 mM, and 32 mM) for another 24 h in order to reduce the silver ions into silver nanoparticles. Here, the color of the swollen hydrogel immediately turned dark brown, which indicates the formation of silver nanoparticles. Finally, the swollen hydrogel loaded with silver nanoparticles was washed with distilled water several times, dried in an oven at 50 °C, ground into a fine powder, and analyzed using multiple analytical characterization techniques. The prepared samples are noted (PPA/Ag1, PPA/Ag2, PPA/Ag3, and PPA/Ag4) in the upcoming sections.

2.3 Characterization

2.3.1 UV–Vis measurement

UV-Visible spectroscopy was used to perform preliminary characterization of the formed silver nanoparticles in the swollen hydrogel. Because of their surface plasmon resonance (SPR), silver nanoparticles possess unique and tunable optical properties that depend on the form, size, and size distribution of the nanoparticles [39]. Well-dispersed samples of gels loaded with AgNPs in distilled water (10 mg/ml) for 10 days were centrifuged at 3000 rpm for 10 min and used to measure the absorption spectra. The distilled water was used as a blank solution. Absorption measurements were recorded on a SECOMAM Uviline 9600 spectrophotometer with a scanning range of 200–800 nm.

2.3.2 FTIR spectroscopy

FTIR analysis of pure hydrogel and hydrogel loaded with AgNPs was recorded on a Cary 630 FTIR spectrometer in the range of 400–4000 cm^{-1} to study the modifications that have occurred in the structure of the hydrogel loaded with AgNPs.

2.3.3 X-ray diffraction (XRD)

This analysis was performed by using a Rigaku Miniflex 600 diffractometer in the range $05° < 2\theta < 80°$ to identify the structure of AgNPs within the hydrogel. By using the Scherrer formula with the full width at half maximum intensity (FWHM), it was possible to calculate the crystallite size [40].

$$D = \frac{K\lambda}{\beta \cos \theta} \quad (1)$$

where "*k*" represents the form factor (0.9), "*D*" represents the crystallite size, "β" denotes the full width at half maximum (FWHM), and "θ" represents the diffraction angle.

2.3.4 Scanning electron microscopy (SEM)

The JEOL JSM 840A (Japan) scanning electron microscope was used for taking the surface morphology images of the prepared AgNPs-loaded gels and pure gels. SEM specimens were prepared by placing 2–3 drops of gels/Ag solution on a silicon wafer and drying in air.

2.4 Photocatalytic activity of gels/Ag NPs

The catalytic activity of different samples (PPA/Ag1, PPA/Ag2, PPA/Ag3, and PPA/Ag4) was evaluated by the photocatalytic degradation of rose bengal dye under sunlight. To start the catalytic degradation process, an aqueous solution of R.B dye (3.10^{-5} M) was prepared with double distilled water. Then, 30 mg of the prepared samples were put into beakers containing 30 ml of dye solution. After various periods of time (0 min, 15 min, 30 min, 60 min, 90 min, and 120 min), 10 ml of the suspension was withdrawn from the medium, centrifuged at 3000 rpm for 10 min to

separate the solids, and the supernatant was finally analyzed by an ultraviolet–visible (UV–Vis) spectrophotometer at λ_{max} = 542 nm wavelength. The percentage degradation (D%) of the R.B. dye was calculated through the following equation [41].

$$D\% = \left(A_0 - A_t\right)/A_0 \times 100 \quad (2)$$

where $(A_o - A_t)$ represents the difference between the first and last absorbance of the R.B dye at its maximum wavelength. At the same time, A_o is the absorbance of R.B. dye before the degradation process begins.

Note that PPA/Ag1, PPA/Ag2, PPA/Ag3, and PPA/Ag4 are assigned to the prepared samples at different concentrations of Ag-loaded PPA (2 mM, 5 mM, 10 mM, and 16 mM), respectively.

2.5 Antibacterial activity

To investigate the antimicrobial effect of the prepared samples. Three types of bacterial strains *Pseudomonas aeruginosa ATCC 27853* (*P. aeruginosa*), *Escherichia coli ATCC 25922* (*E. coli*), and *Staphylococcus aureus ATCC 25923* (*S. aureus*) were chosen for the antibacterial activity test. The agar well diffusion assay method was used; it is a commonly used method to assess antimicrobial activity [42]. The strains were first cultured in nutrient agar (composition: agar 15 g, peptone 5 g, sodium chloride (NaCl) 5 g, beef extract 1.5 g, and yeast extract 1.5 g, prepared in 1 L distilled water, pH 7.0) and then inoculated in Petri plates containing Mueller Hinton agar. After that, the prepared samples (in the swollen form) were put into the wells. Finally, the plates were incubated at 37 °C, and the inhibition zones were measured after 24 h of incubation. The test was conducted with three replications, and various antibiotics were also included in the test as positive controls, particularly gentamicin, ofloxacin, cefixime, and cotrimoxazole.

3 Results and discussion

Several recent studies have focused on the synthesis of hydrogels containing metal nanoparticles [28, 43] because of their explicit involvement in various biomedical uses, such as bio-catalysis, contrast imaging, cell labeling, and antibacterial applications [44]. The present study provided an easy procedure for integrating AgNP within potassium polyacrylate hydrogel by immersing dry PPA hydrogel in $AgNO_3$ aqueous solution and transferring the gel to $NaBH_4$ aqueous solution for the reduction reaction, as was demonstrated in the previous section. Figure 1 illustrates the steps of producing AgNPs in the hydrogel networks. The benefit of this procedure is that it allows the hydrogel to hold a lot of Ag^+ ions and facilitates their reduction. Thus, it affords an evenly distributed spread of AgNPs within hydrogel networks and gives them excellent stabilization as well. Consider that PPA chains work effectively as stabilizing agents.

3.1 UV–Vis spectroscopy

UV-Vis spectroscopy was the first technique conducted to examine the integration of AgNPs in the hydrogel. The UV-Vis spectra of Ag-embedded gels show an explicit absorption peak at around 419 nm (Fig. 2a) due to the surface plasmon resonance effect caused by the quantum size of AgNPs [45, 46], but neither the pure hydrogel nor the $AgNO_3$ exhibited an absorption peak at this wavelength. In addition, it is essential to note that there were no other absorption peaks around 335 nm and 560 nm wavelengths (Fig. 2a), which refers to the absence of AgNPs aggregation [29]. The presence of silver ions (Ag^+) in the solution causes the absorption band in the aqueous solution of silver nitrate. Silver ions (Ag^+) and nitrate ions (NO^{3-}) are produced when silver nitrate ($AgNO_3$) dissolves in water. The distinctive absorption band seen in the solution's UV-Vis spectra is caused by the silver ions. The indirect optical bandgap of the silver nitrate ($AgNO_3$) sample

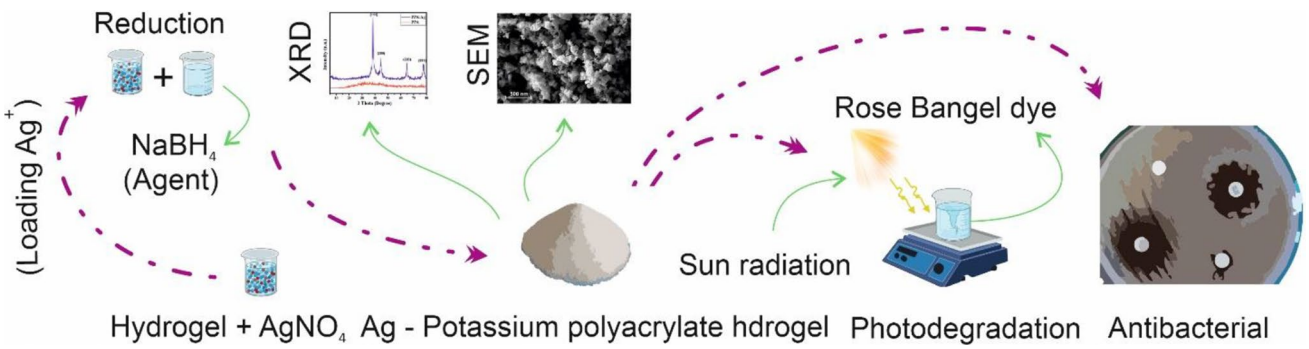

Fig. 1 A schematic illustration of potassium polyacrylate hydrogel-loaded AgNPs preparation

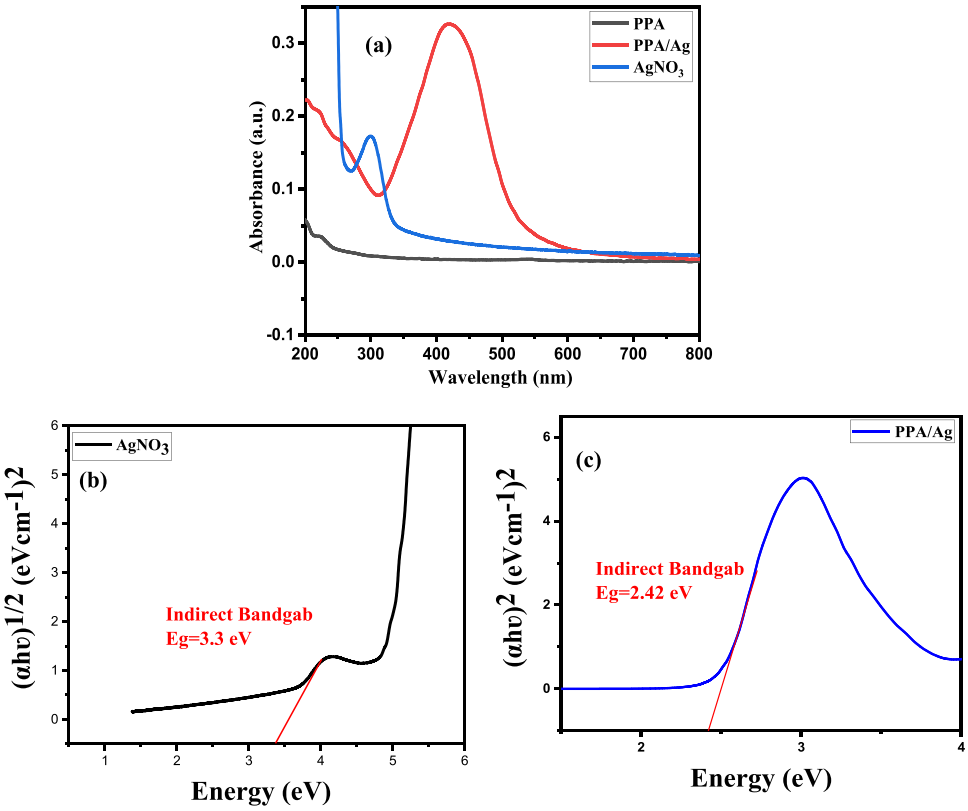

Fig. 2 UV-Vis spectra of (**a**) $AgNO_3$, pure PPA and the prepared PPA/Ag, (**b**) bandgap of $AgNO_3$, and (**c**) bandgap of PPA/Ag

was determined to be 3.3 eV (Fig. 2b). However, upon the introduction of PPA, the bandgap was observed to decrease to 2.42 eV (Fig. 2c). This reduction in bandgap renders the PPA/Ag composite material highly suitable for use in the process of photocatalytic degradation.

3.2 FTIR spectroscopy

Figure 3 represents Fourier transform infrared spectra of the pure PPA hydrogel and silver nanoparticles-loaded PPA hydrogel sample. The FTIR spectra of PPA hydrogel showed a substantial broadening of the O-H stretching of PPA at 3376–3235 cm^{-1}. The peaks at 2929 cm^{-1} and 1446 cm^{-1} correspond to C-H asym./sym stretching and C-H bending. The apparent peaks at 2363 cm^{-1}, 2117 cm^{-1}, and 1654 cm^{-1} are due to the O=C=O, C≡C and C=C stretching, respectively [47], and 1401 cm^{-1} is assigned to the O-H bending of the carboxylic group. The observed peaks at (1550 cm^{-1}, 1222 cm^{-1}) and 1319 cm^{-1} are due to N-H group bending (Coates, 2000) and C-N group stretching, respectively. The obtained peaks at 1162 cm^{-1} and 1058 cm^{-1} are due to the stretching of C-O of primary alcohol [28]. The FTIR analysis of AgNPs-loaded hydrogel revealed similar peaks to PPA hydrogel, but differences in the intensity and frequency of various peaks were observed (Fig. 3). The presence of AgNPs in the hydrogel caused a decrease in the bending intensity of

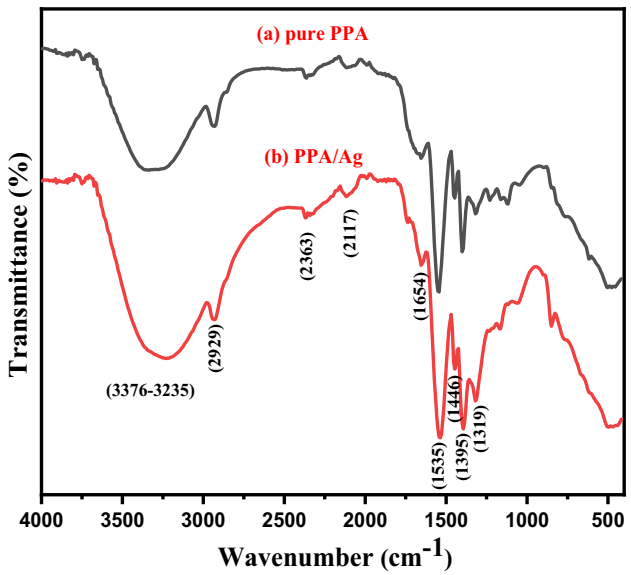

Fig. 3 Fourier transform infrared (FTIR) spectra of (**a**) pure PPA hydrogel and (**b**) silver nanoparticles-loaded PPA hydrogel

O-H and N-H peaks and a considerable shifting of these peaks from 1401 cm^{-1} and 1550 cm^{-1} to 1395 cm^{-1} and 1535 cm^{-1} respectively. The intensity is always dependent on the molecular weight of the PPA hydrogel; the more AgNPs loaded in the PPA hydrogel, the lower the

intensity revealed. The weakening intensity refers to the silver bonding to oxygen and nitrogen, which raises the molecular weight of the compound (PPA/Ag) and makes it heavier than before, resulting in a decline in intensity. The shifting of O-H and N-H bending towered minimum frequency, referring to the weakening of intermolecular hydrogen bonds due to the existence of AgNPs [14]. Furthermore, the peak of the N-H group bending at 1222 cm^{-1} has disappeared, and a new peak was found at 849 cm^{-1} which supports the possibility of forming a new bond linking AgNPs with nitrogen.

Moreover, O-H stretching at 3376–3235 cm^{-1} in PPA showed less intensity in PPA loaded with AgNPs, which would also support the possibility of interaction between oxygen and Ag. These findings offer substantial proof that AgNPs were successfully incorporated into the PPA hydrogel.

3.3 XRD analysis

X-ray diffraction technique was also employed to confirm the integration of AgNPs in the PPA hydrogel networks. From Fig. 4, there were any peaks appear in the XRD pattern of the pure PPA hydrogel, while the XRD pattern of PPA/Ag shows four diffraction peaks found at 38.43°, 44.65°, 64.85° and 77.88° are attributed to the diffraction planes (111), (200), (220), and (311) of the face-centered cubic (fcc) of the AgNPs, respectively, which definitely proved the formation of AgNPs within the hydrogel structure. The crystallite sizes of the PPA/Ag were 31.83 nm, according to the Scherrer formula.

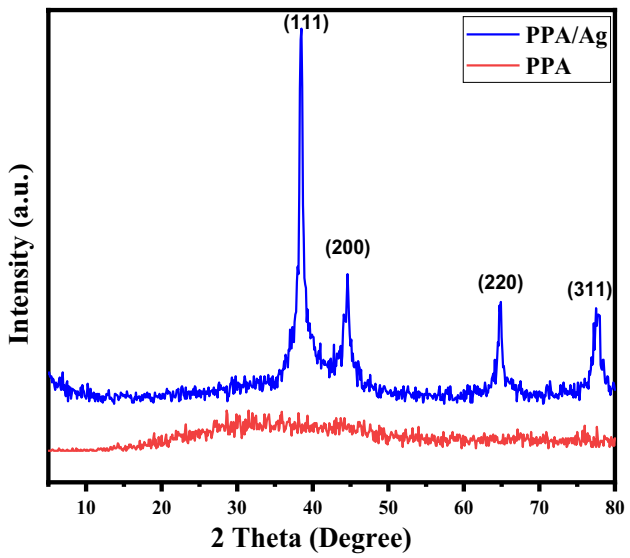

Fig. 4 XRD diffraction patterns of pure PPA and PPA loaded with AgNPs (PPA/Ag)

3.4 Scanning electron microscopy

The SEM images of plain PPA hydrogel are depicted in Fig. 5. Figure 5 shows the morphology of the PPA hydrogel as it was an irregularly shaped nanogel. Fig. 6 appears the EDX analysis of hydrogel containing AgNPs. The EDX quantitative analysis contains 60.48% and 34.12% for Ag and carbon elements, respectively, confirming the presence of AgNPs in the PPA hydrogel.

3.5 Photocatalytic degradation study

Photocatalytic activity arises as a result of the photocatalyst's interaction with UV irradiation, which produces extremely reactive hydroxyl radicals, which are thought to be the main species responsible for oxidation [48, 49].

Water in the surrounding media produces hydroxyl radicals (•OH) when a photocatalyst is exposed to UV light. These hydroxyl radicals are a reliable sign of the catalyst's photocatalytic activity [50].

Hydroxyl radicals (•OH) react with organic molecules, minerals, and other substances in the medium around the catalyst, breaking chemical bonds and forming new compounds as a result. This reaction is a strong sign of oxidation in the system [51].

The degradation of an anionic dye solution in the presence of the prepared samples (PPA/Ag1, PPA/Ag2, PPA/Ag3, and PPA/Ag4) was studied in this work; the samples acted as catalysts in this degradation process. Rose bengal (R.B.) (Fig. 7) was used as a model dye in this study, and the degradation process was investigated under irradiation of visible sunlight from 11:30 a.m. to 1:30 p.m. Rose bengal (R.B.) dye has a big absorption peak at 542 nm, which represents its maximum wavelength. Figure 7 depicts the UV-visible spectra of dye degradation as a function of time as well as the degradation efficiency of various catalysts. It was obviously observed that after adding the catalysts, the

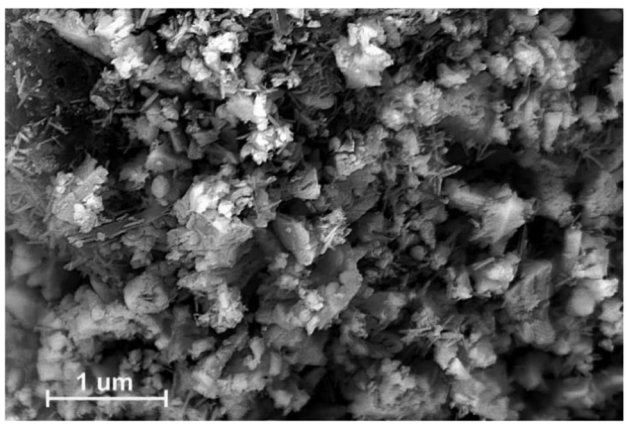

Fig. 5 SEM images of pure PPA hydrogel

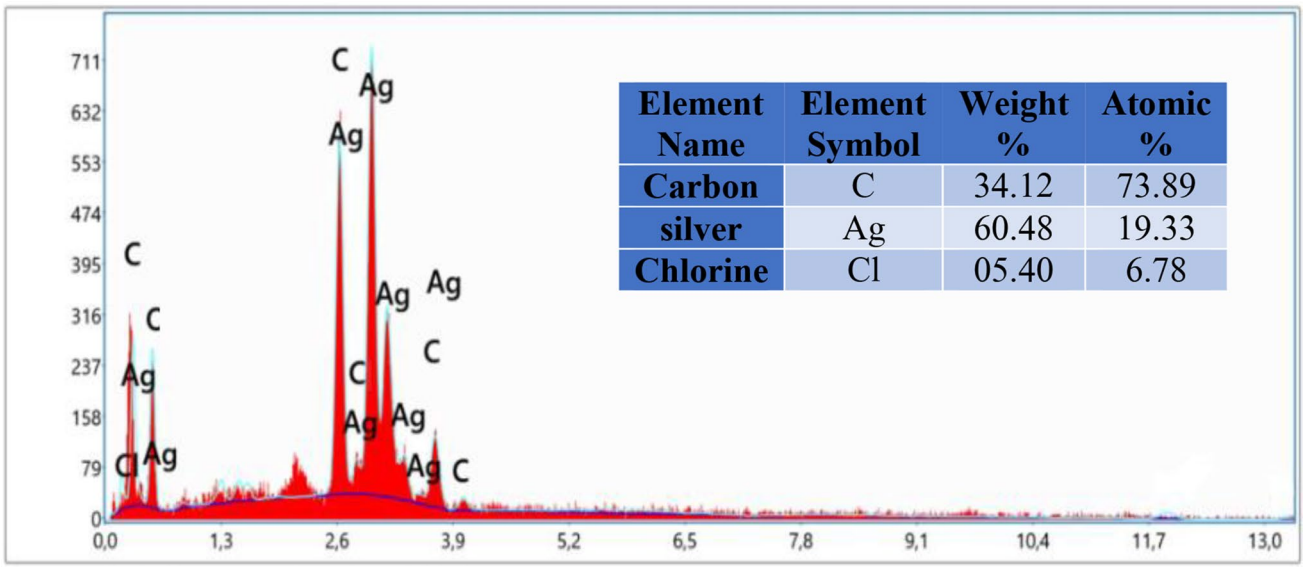

Element Name	Element Symbol	Weight %	Atomic %
Carbon	C	34.12	73.89
silver	Ag	60.48	19.33
Chlorine	Cl	05.40	6.78

Fig. 6 EDX of AgNPs-loaded gels

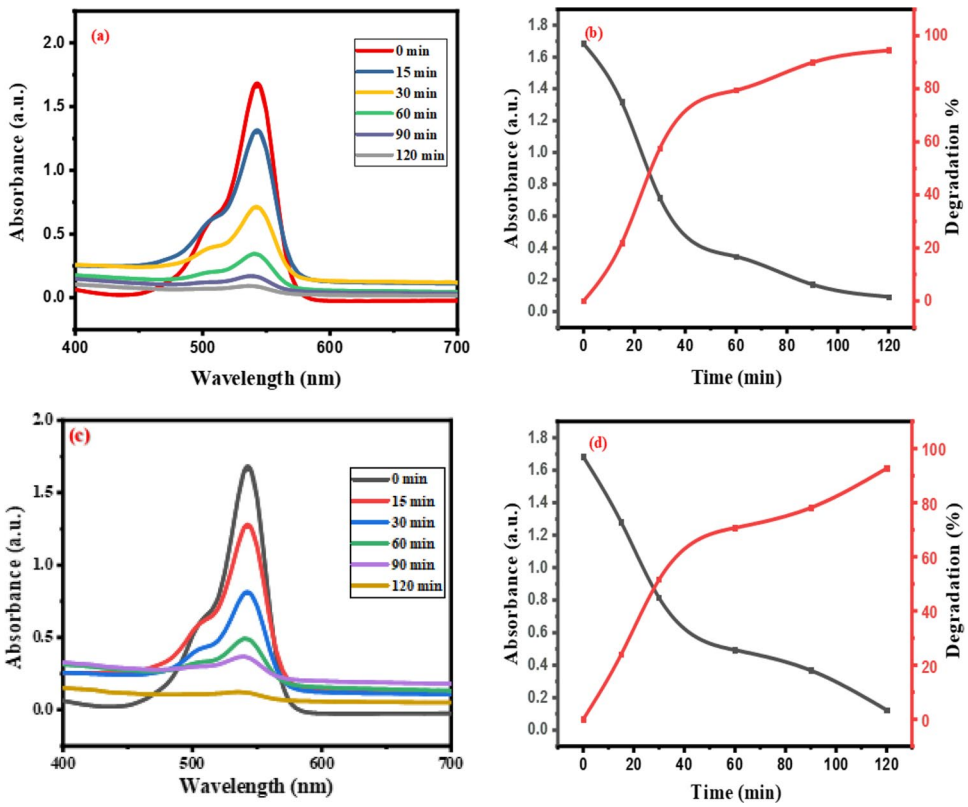

Fig. 7 UV-Vis spectra of the degradation of R.B. (concentration 3.10^{-5} M, catalyst dose 30 mg) dye in the presence of (**a**) PPA/Ag1, (**c**) PPA/Ag2, (**e**) PPA/Ag3, and (**g**) PPA/Ag4 and D% in the presence of (**b**) PPA/Ag1, (**d**) PPA/Ag2, (**f**) PPA/Ag3, and (**h**) PPA/Ag4. Note: PPA/Ag1, PPA/Ag2, PPA/Ag3, and PPA/Ag4 are assigned to the prepared samples at different concentrations of Ag-loaded PPA (2 mM, 5 mM, 10 mM, and 16 mM), respectively

color of the R.B aqueous solution started to convert from pink to transparent, and its absorption intensity at $\lambda_{max} = 542$ nm began to decrease with increasing time, which confirmed the effective photocatalytic degradation of R-B in the presence of the catalysts.

The calculated degradation efficiencies showed almost similar percentages for all the prepared catalysts. Also, the results showed that the highest values of D% were achieved after 120 min of exposing R.B. dye to visible sunlight in the presence of the catalysts. The results are listed in Table 1.

Fig. 7 (continued)

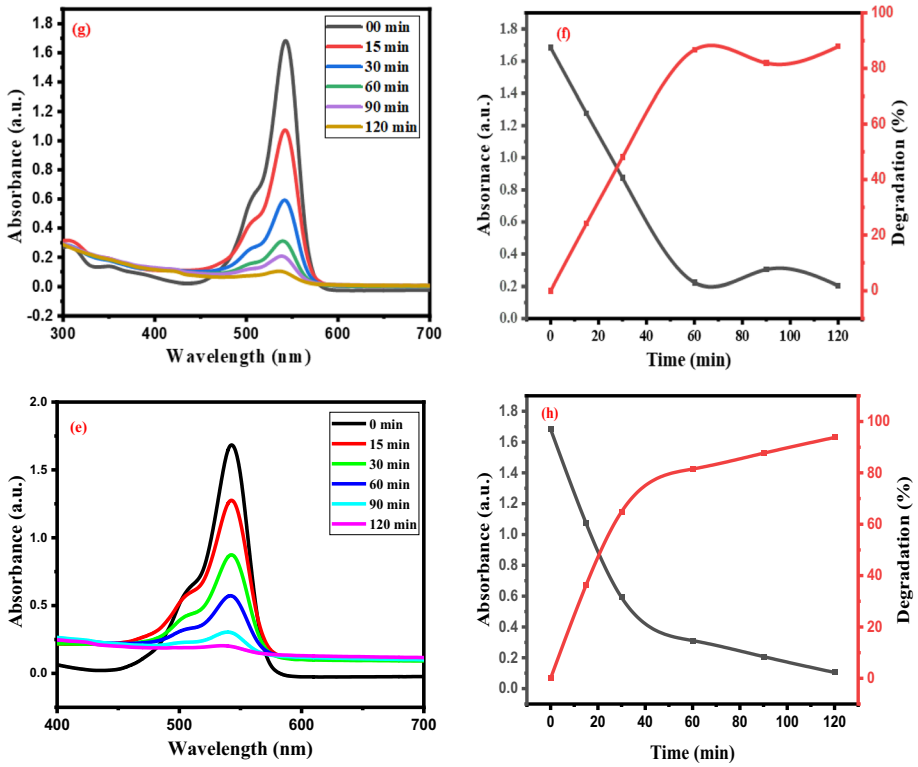

Table 1 Values of degradation efficiency, correlation coefficient, and rate constant

Catalysts	D (%)	R^2	k (min^{-1})
PPA/Ag1	94	0.991	0.025
PPA/Ag2	93	0.961	0.020
PPA/Ag3	88	0.992	0.018
PPA/Ag4	95	0.972	0.022

The rate constant of the degradation reaction was achieved by the Langmuir-Hinshelwood (L-H) model. This model (Eq. (3)) is the most commonly used equation to define photocatalytic reactions, study kinetics, and establish the relationship between initial dye concentration and initial rate degradation.

$$1/K = 1/\left(Kc * K_{L-H}\right) + C_0/kc \tag{3}$$

where C_0 is the dye's initial concentration (mg/L), k_c is the reaction rate constant (mg/L min), and $K_{L\text{-}H}$ is the Langmuir-Hinshelwood adsorption equilibrium constant (L/mg).

The rate of reaction may be defined as proportional to the decrease in the concentration of a reactant per time and the increase in the concentration of a product per time. Equation (4) represents the rate expression of the reaction.

$$r = -dC/dt = kC \tag{4}$$

In the case of low concentration of the R.B. dye, Eq. (4) can be integrated to give a linear equation as follows :[52, 53]

$$-\ln(C/C0) = \ln\left(C_0/C\right) = kt \tag{5}$$

where C_0 is the initial concentration of R.B. dye and C is the concentration of R.B. dye at any time (t) of irradiation. k is the pseudo-first-order rate constant (min^{-1}); it can be obtained from the slope of the straight line by plotting $\ln(C_0/C)$ versus irradiation time (min). Figure 8 shows the plots of $\ln(C_0/C_t)$ values against irradiation time for the reactions in this experiment. The values of the rate constant k and the correlation coefficient R^2 are tabulated in Table 1.

According to Fig. 9, it is noticed that the photocatalytic degradation was performed with good performance. In addition, the results showed that the prepared PPA/Ag catalysts provided considerable rate constant k values for R.B. degradation, and they were pretty similar, except PPA/Ag1 provided a slightly lesser value of k than the other catalysts. Moreover, when large values of the correlation coefficient are obtained in an experiment, this indicates that the interactions follow pseudo-first-order kinetics. Pseudo-first-order kinetics means that reactions follow the speed of a true first-order reaction in the initial stages of the reaction, but slow down significantly in the later stages of the reaction.

Figure 10 presents a schematic representation of the potential mechanism involved in the degradation of RB dye using

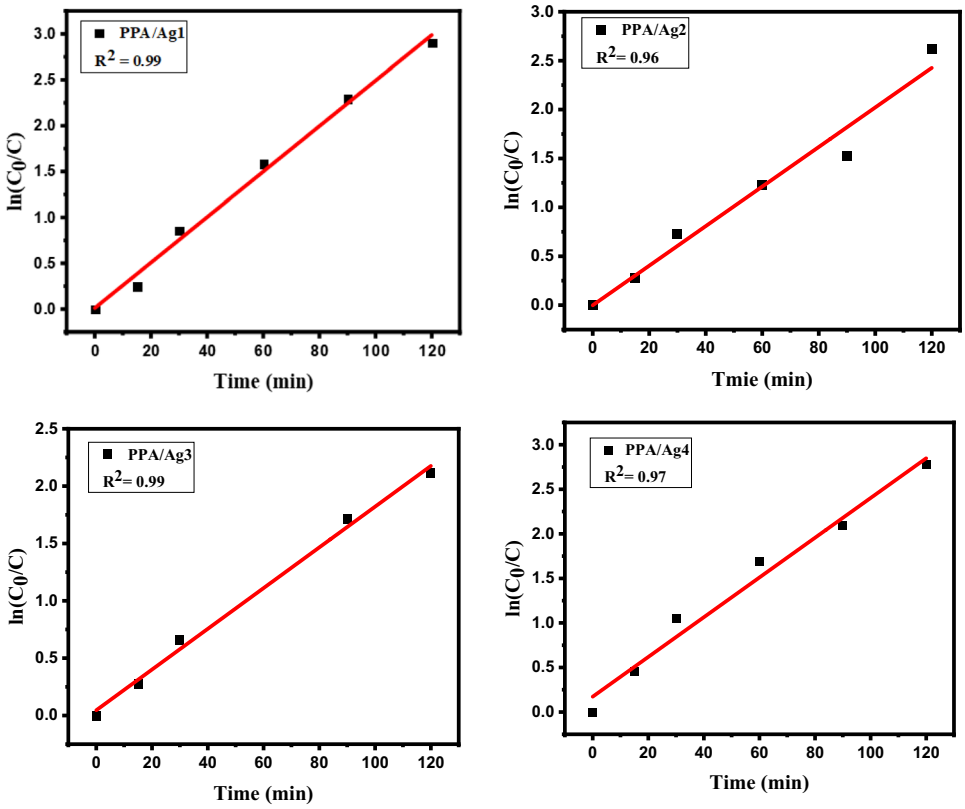

Fig. 8 Langmuir-Hinshel wood kinetics for rose bengal in the presence of different catalysts

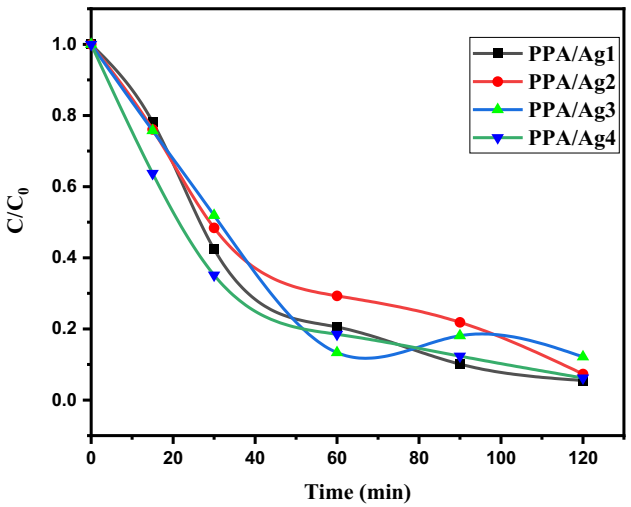

Fig. 9 C/C_0 plots of R.B. versus irradiation time in the presence of catalysts

PPA/Ag. As shown in Eqs. (6)–(10), when exposed to light, the high surface area of PPA/Ag facilitates the generation of electron-hole (e^--h^+) pairs between the conduction band (CB) and valence band (VB) of PPA/Ag, leading to the degradation of RB dye [54]. Initially, the photogenerated electrons (e^-) in the CB of PPA/Ag migrate toward the surface and are scavenged by oxygen (O_2) to form superoxide anion (O_2^-) and simultaneously react with protons to produce hydroperoxyl radicals (HOO•). On the other hand, the photogenerated holes (h^+) in the VB migrate to the backside of the PPA/Ag surface and react with either water (H_2O) or hydroxide (OH^-) ions to generate active species like hydroxyl radicals (OH•). These processes are facilitated by the efficient separation of photogenerated electron-hole pairs, which significantly contribute to the degradation of RB. The following steps are potential for the degradation of RB [12]:

$$\mathrm{PPA/Ag} + h\nu \rightarrow e^- + h^+ \quad (6)$$

$$\mathrm{O_2 + e^-\bullet_2^- + H+ \rightarrow \bullet OOH} \quad (7)$$

$$\mathrm{e^- + \bullet OOH \rightarrow H_2O_2} \quad (8)$$

$$\mathrm{H_2O_2 + e- \rightarrow HO\bullet + OH^-} \quad (9)$$

$$\mathrm{dye + \bullet OH + \bullet O_2 \rightarrow Degradation\ products + CO_2 + H_2O} \quad (10)$$

3.6 Antibacterial activity

The PPA hydrogel and all the prepared samples of AgNPs-loaded hydrogel (PPA/Ag1, PPA/Ag2, PPA/Ag3, and PPA/Ag4) were tested against three types of microorganisms: *P.*

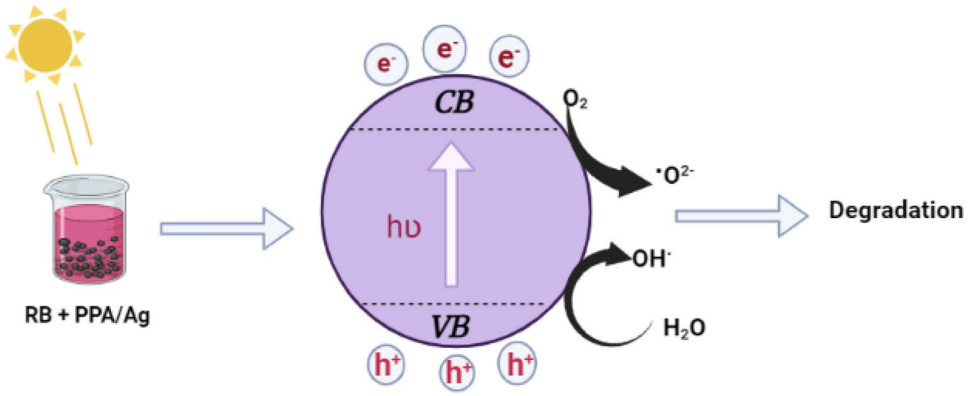

Fig. 10 Proposed mechanism for the photocatalytic degradation of RB dye using PPA/Ag under solar light irradiation

Table 2 Samples' inhibition zones (mm) of the antibacterial activity test

Samples	*P. aeruginosa*	*E. coli*	*S. aureus*
PPA/Ag1	18.5	21	11
PPA/Ag2	13	12	13
PPA/Ag3	14	12	15
PPA/Ag4	14	13	12.5

aeruginosa, *E. coli*, and *S. aureus*; the test was conducted with three replications. According to Table 2, all the samples embedded with AgNPs presented a significant antibacterial effect against the different types of microorganisms, while the pure hydrogel presented no effect. Furthermore, PPA/Ag1 showed a magnificent inhibition zone against *P. aeruginosa* and *E. coli*, as observed in Fig. 11. Moreover, as a comparison between the prepared samples and the different antibiotics used in this test (Table 3), PPA/Ag1 presented relatively equal inhibition zones against *E. coli* and *P. aeruginosa* bacterial strains when compared with OFX and larger inhibition zones than the other antibiotics (Fig. 12). The samples (PPA/Ag2, PPA/Ag3, and PPA/Ag4) showed better antibacterial effects than CFM against *S. aureus*. The main antimicrobial mechanisms of action could be due to the fact that AgNPs release from PPA hydrogel and adhere to microbial cells, penetrate into them, and attack both the respiratory chain and cell division by interacting with phosphors and sulfur-containing compounds in the bacterial cells, leading to their death [8, 55].

4 Conclusion

The used approach enables easy integration of silver nanoparticles in potassium polyacrylate hydrogel. The formation of silver nanoparticles in the hydrogel networks was confirmed by various analyzing techniques, including UV-Vis spectrophotometry, FTIR spectroscopy, XRD, and SEM. Furthermore, the prepared PPA/Ag samples presented high efficiency in the photocatalytic degradation of rose bengal dye, where the highest degradation efficiency reached 95% for PPA/Ag4, followed by PPA/Ag1, then PPA/Ag2, and finally PPA/Ag3 with 94%, 93%, and 88%, respectively. In

Table 3 Antibiotics' inhibition zones (mm) of antibacterial activity test

Antibiotics	*P. aeruginosa*	*E. coli*	*S. aureus*
Cefixime	6	9	13
Ofloxacin	21	21	23
Cotrimoxazole	6	6	17
Gentamicin	/	16	/

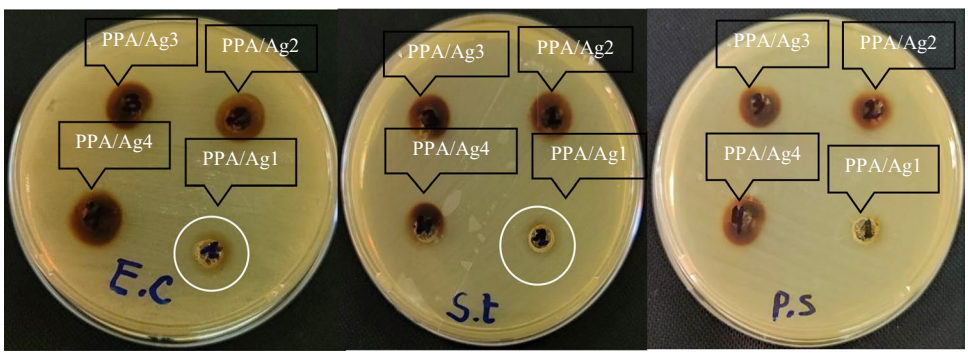

Fig. 11 Antibacterial activity effect of the prepared samples against the different strains

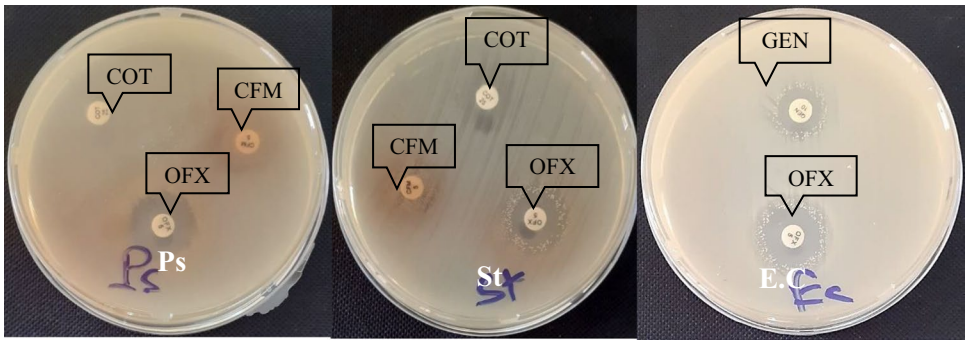

Fig. 12 Antibacterial activity effect of the antibiotics against the different strains

addition, broad inhibition zones were observed against *E. coli*, *P. aeruginosa*, and *S. aureus* microorganism strains, which evidenced excellent antimicrobial effects for the prepared PPA/Ag samples. According to the obtained results, these Ag-loaded PPA hydrogel nanocomposites can be successfully used in wastewater treatments as catalysts and in medical fields such as drug carriers and wound healing.

Acknowledgements The authors wish to thank the Directorate General for Scientific Research and Technological Development DGRSDT, Algeria, for financial support.

Authors' contribution Conceptualization: A.B., S.M., A.BOUAFIA., H.A.M.M., H.G.G., and S.E.L.; data curation: A.B., S.M., A.BOUAFIA., H.G.G., and S.E.L.; formal analysis: A.B., S.M., A.BOUAFIA., and H.A.M.M.; investigation: A.BOUAFIA., S.M., S.E.L., and H.A.M.M.; methodology: A.BOUAFIA., H.A.M.M., H.G.G., and S.E.L.; project administration: S.M., A.BOUAFIA., H.G.G., and S.E.L.; resources: A.B., S.M., S.E.L., and A.BOUAFIA.; software: A.BOUAFIA. and H.A.M.M.; supervision: S.M. and A.B.; validation: A.BOUAFIA., A.B., and S.E.L.; visualization: A.BOUAFIA. and S.E.L.; writing – original draft: A.B., A.BOUAFIA., H.G.G., S.E.L., H.A.M.M., and S.M.; writing – review and editing: A.B., S.M., H.G.G., H.A.M.M., and S.E.L.; the authors have read and agreed to the published version of the manuscript.

Data Availability All data generated or analysed during this study are included in this published article.

Declarations

Ethical approval Not applicable.

Competing interests The authors declare no competing interests.

References

1. Li D, Wang F, Zhang X, Liang L, Sun J (2014) The efficient removal of organic pollutant over magnetic mesoporous polymer. J Porous Mater 21(5):811–817
2. Jiao T, Guo H, Zhang Q, Peng Q, Tang Y, Yan X, Li B (2015) Reduced graphene oxide-based silver nanoparticle-containing composite hydrogel as highly efficient dye catalysts for wastewater treatment. Sci Rep 5(1):1–12
3. Althamthami M, Temam EG, Temam HB, Hasan GG, Malfi N (2022) Influence of hole-scavenger and different withdrawn speeds on photocatalytic activity of Co3O4 thin films under sunlight irradiation. Ceram Int 48(21):31570–31578
4. Bouafia A, Laouini SE, Khelef A, Tedjani ML, Guemari F (2021) Effect of ferric chloride concentration on the type of magnetite (Fe3O4) nanoparticles biosynthesized by aqueous leaves extract of artemisia and assessment of their antioxidant activities. J Clust Sci 32(4):1033–1041. https://doi.org/10.1007/s10876-020-01868-7
5. Bouafia A, Laouini SE, Tedjani ML, Ali GAM, Barhoum A (2021) Green biosynthesis and physicochemical characterization of Fe3O4 nanoparticles using Punica granatum L. fruit peel extract for optoelectronic applications. Textile Res J 92. https://doi.org/10.1177/00405175211006671
6. Laouini SE, Bouafia A, Soldatov AV, Algarni H, Tedjani ML, Ali GAM, Barhoum A (2021) Green synthesized of Ag/Ag2O nanoparticles using aqueous leaves extracts of Phoenix dactylifera L. and their azo dye photodegradation. Membranes 11(7):468
7. Murugadoss G, Kumar DD, Kumar MR, Venkatesh N, Sakthivel P (2021) Silver decorated CeO2 nanoparticles for rapid photocatalytic degradation of textile rose bengal dye. Sci Rep 11(1):1–13
8. Daoudi H, Bouafia A, Meneceur S, Laouini SE, Belkhalfa H, Lebbihi R, Selmi B (2022) Secondary metabolite from nigella sativa seeds mediated synthesis of silver oxide nanoparticles for efficient antioxidant and antibacterial activity. J Inorg Organomet Polym Mater 32(11):4223–4236. https://doi.org/10.1007/s10904-022-02393-y
9. Terea H, Selloum D, Rebiai A, Bouafia A, Ben Mya O (2023) Preparation and characterization of cellulose/ZnO nanoparticles extracted from peanut shells: effects on antibacterial and antifungal activities. Biomass Convers Biorefin. https://doi.org/10.1007/s13399-023-03959-7
10. Patra N, Kar D, Pal A, Behera A (2018) Antibacterial, anticancer, anti-diabetic and catalytic activity of bio-conjugated metal nanoparticles. Adv Nat Sci: Nanosci Nanotechnol 9(3):035001
11. Slavin YN, Asnis J, Hńfeli UO, Bach H (2017) Metal nanoparticles: understanding the mechanisms behind antibacterial activity. J Nanobiotechnology 15:1–20
12. Mohammed Mohammed HA, Souhaila M, Eddine LS, Hasan GG, Kir I, Mahboub MS (2023) A novel biosynthesis of MgO/PEG nanocomposite for organic pollutant removal from aqueous solutions under sunlight irradiation. Environ Sci Pollut Res:1–10
13. Zheng ALT, Phromsatit T, Boonyuen S, Andou Y (2020) Synthesis of silver nanoparticles/porphyrin/reduced graphene oxide hydrogel as dye adsorbent for wastewater treatment. FlatChem 23:100174
14. Porchezhiyan V, Noorjahan S (2016) Fabrication of a versatile chitosan nanocomposite hydrogel impregnated with biosynthesized silver nanoparticles using Sapindus mukorossi: characterization and applications. RSC Adv 6(98):95564–95573
15. Hasan GG, Khelef A, Chaabia N, Tedjani ML, Althamthami M (2023) Electrochemical deposition of Ag nanoparticles on

ITO-coated glass: effect of different cyclic voltammetry scan rates on Ag deposition. Ferroelectrics 602(1):121–134
16. Ali F, Khan SB, Kamal T, Anwar Y, Alamry KA, Asiri AM (2017) Bactericidal and catalytic performance of green nanocomposite based-on chitosan/carbon black fiber supported monometallic and bimetallic nanoparticles. Chemosphere 188:588–598
17. Hebeish A, Hashem M, Abd El-Hady M, Sharaf S (2013) Development of CMC hydrogels loaded with silver nano-particles for medical applications. Carbohydr Polym 92(1):407–413
18. Hoffman AS (2012) Hydrogels for biomedical applications. Adv Drug Deliv Rev 64:18–23
19. Ciolacu DE, Suflet DM (2018) Cellulose-based hydrogels for medical/pharmaceutical applications. In: Biomass as renewable raw material to obtain bioproducts of high-tech value. Elsevier, pp 401–439
20. Bae J, Park J, Kim S, Cho H, Kim HJ, Park S, Shin D-S (2020) Tailored hydrogels for biosensor applications. J Ind Eng Chem 89:1–12
21. Das D, Prakash P, Rout PK, Bhaladhare S (2021) Synthesis and characterization of superabsorbent cellulose-based hydrogel for agriculture application. Starch-Stärke 73(1-2):1900284
22. Gopinathan J, Noh I (2018) Click chemistry-based injectable hydrogels and bioprinting inks for tissue engineering applications. J Tissue Eng Regen Med 15:531–546
23. Wu J, Guo J, Linghu C, Lu Y, Song J, Xie T, Zhao Q (2021) Rapid digital light 3D printing enabled by a soft and deformable hydrogel separation interface. Nature communications 12(1):6070
24. Shah LA, Farooqi ZH, Naeem H, Shah SM, Siddiq M (2013) Synthesis and characterization of poly (N-isopropylacrylamide) hybrid microgels with different cross-linker contents. J Chem Soc Pak 35:1522–1529
25. Shah LA, Ambreen J, Bibi I, Sayed M, Siddiq M (2016) Silver nanoparticles fabricated hybrid microgels for optical and catalytic study. J Chem Soc Pak 38(5)
26. Kamal T, Khan MSJ, Khan SB, Asiri AM, Chani MTS, Ullah MW (2020) Silver nanoparticles embedded in gelatin biopolymer hydrogel as catalyst for reductive degradation of pollutants. J Polym Environ 28:399–410
27. Eid M (2011) Gamma radiation synthesis and characterization of starch based polyelectrolyte hydrogels loaded silver nanoparticles. J Inorg Organomet Polym Mater 21:297–305
28. Liu Y, Li F, Guo Z, Xiao Y, Zhang Y, Sun X, Zhe T, Cao Y, Wang L, Lu Q (2020) Silver nanoparticle-embedded hydrogel as a photothermal platform for combating bacterial infections. J Chem Eng 382:122990
29. Mohan YM, Vimala K, Thomas V, Varaprasad K, Sreedhar B, Bajpai S, Raju KM (2010) Controlling of silver nanoparticles structure by hydrogel networks. J Colloid Interface Sci 342(1):73–82
30. Mohan YM, Lee K, Premkumar T, Geckeler KE (2007) Hydrogel networks as nanoreactors: a novel approach to silver nanoparticles for antibacterial applications. Polymer 48(1):158–164
31. Amor IB, Hemmami H, Laouini SE, Temam HB, Zaoui H, Barhoum A (2023) Biosynthesis MgO and ZnO nanoparticles using chitosan extracted from Pimelia Payraudi Latreille for antibacterial applications. World J Microbiol Biotechnol 39(1):19
32. Shivakumar M, Nagashree K, Yallappa S, Manjappa S, Manjunath K, Dharmaprakash M (2017) Biosynthesis of silver nanoparticles using pre-hydrolysis liquor of Eucalyptus wood and its effective antimicrobial activity. Enzyme Microb Technol 97:55–62
33. Abdullah JAA, Jiménez-Rosado M, Benítez JJ, Guerrero A, Romero A (2022) Biopolymer-based films reinforced with FexOy-nanoparticles. Polymers 14(21):4487
34. Koduru JR, Kailasa SK, Bhamore JR, Kim K-H, Dutta T, Vellingiri K (2018) Phytochemical-assisted synthetic approaches for silver nanoparticles antimicrobial applications: a review. Adv Colloid Interface Sci 256:326–339
35. Kailasa SK, Borse S, Koduru JR, Murthy Z (2021) Biomolecules as promising ligands in the synthesis of metal nanoclusters: sensing, bioimaging and catalytic applications. Trends Environ Anal Chem 32:e00140
36. Jin P, Mattelaer V, Yuan S, Bassyouni M, Simoens K, Zhang X, Ceyssens F, Bernaerts K, Dewil R, Van der Bruggen B (2022) Hydrogel supported positively charged ultrathin polyamide layer with antimicrobial properties via Ag modification. Sep Purif Technol 284:120295. https://doi.org/10.1016/j.seppur.2021.120295
37. Oksińska MP, Magnucka EG, Lejcuś K, Jakubiak-Marcinkowska A, Ronka S, Trochimczuk AW, Pietr SJ (2019) Colonization and biodegradation of the cross-linked potassium polyacrylate component of water absorbing geocomposite by soil microorganisms. Appl Soil Ecol 133:114–123
38. Liu X, Chan Z (2015) Application of potassium polyacrylate increases soil water status and improves growth of bermudagrass (Cynodon dactylon) under drought stress condition. Sci Hortic 197:705–711
39. Mulvaney P (1996) Surface plasmon spectroscopy of nanosized metal particles. Langmuir 12(3):788–800
40. Kir I, Laouini SE, Meneceur S, Bouafia A, Mohammed HAM (2023) Biosynthesis and characterization of novel nanocomposite ZnO/BaMg2 efficiency for high-speed adsorption of AZO dye. Biomass Convers Biorefin 256:326–339
41. Khan MI, Akhtar MN, Ashraf N, Najeeb J, Munir H, Awan TI, Tahir MB, Kabli MR (2020) Green synthesis of magnesium oxide nanoparticles using Dalbergia sissoo extract for photocatalytic activity and antibacterial efficacy. Appl Nanosci 10(7):2351–2364
42. Balouiri M, Sadiki M, Ibnsouda SK (2016) Methods for in vitro evaluating antimicrobial activity: a review. J Pharm Anal 6(2):71–79
43. Jayaramudu T, Varaprasad K, Pyarasani RD, Reddy KK, Akbari-Fakhrabadi A, Carrasco-Sánchez V, Amalraj J (2021) Hydroxypropyl methylcellulose-copper nanoparticle and its nanocomposite hydrogel films for antibacterial application. Carbohydr Polym 254:117302
44. Thomas V, Namdeo M, Murali Mohan Y, Bajpai S, Bajpai M (2007) Review on polymer, hydrogel and microgel metal nanocomposites: a facile nanotechnological approach. J Macromol Sci- Pure Appl Chem 45(1):107–119
45. Zhang J, Xu S, Kumacheva E (2004) Polymer microgels: reactors for semiconductor, metal, and magnetic nanoparticles. J Am Chem Soc 126(25):7908–7914
46. Filippo E, Serra A, Manno D (2009) Poly (vinyl alcohol) capped silver nanoparticles as localized surface plasmon resonance-based hydrogen peroxide sensor. Sens. Actuators B Chem 138(2):625–630
47. Coates J (2000) Interpretation of infrared spectra, a practical approach.
48. Kumar R, Umar A, Kumar G, Akhtar M, Wang Y, Kim S (2015) Ce-doped ZnO nanoparticles for efficient photocatalytic degradation of direct red-23 dye. Ceram Int 41(6):7773–7782
49. Bhatia S, Verma N (2017) Photocatalytic activity of ZnO nanoparticles with optimization of defects. Mater Res Bull 95:468–476
50. Al-Nuaim MA, Alwasiti AA, Shnain ZY (2023) The photocatalytic process in the treatment of polluted water. Chem Pap 77(2):677–701. https://doi.org/10.1007/s11696-022-02468-7
51. Lobo V, Patil A, Phatak A, Chandra N (2010) Free radicals, antioxidants and functional foods: impact on human health. Pharmacogn Rev 4(8):118–126. https://doi.org/10.4103/0973-7847.70902
52. Naeem H, Tofil HM, Soliman M, Hai A, Zaidi SHH, Kizilbash N, Alruwaili D, Ajmal M, Siddiq M (2023) Reduced graphene oxide-zinc sulfide nanocomposite decorated with silver nanoparticles for

wastewater treatment by adsorption, photocatalysis and antimicrobial action. Molecules 28(3). https://doi.org/10.3390/molecules28030926

53. Arshad A, Iqbal J, Siddiq M, Mansoor Q, Ismail M, Mehmood F, Ajmal M, Abid Z (2017) Graphene nanoplatelets induced tailoring in photocatalytic activity and antibacterial characteristics of MgO/graphene nanoplatelets nanocomposites. J Appl Phys 121(2). https://doi.org/10.1063/1.4972970
54. Rahman QI, Ahmad M, Misra SK, Lohani M (2013) Effective photocatalytic degradation of rhodamine B dye by ZnO nanoparticles. Mater Lett 91:170–174
55. Dakal TC, Kumar A, Majumdar RS, Yadav V (2016) Mechanistic basis of antimicrobial actions of silver nanoparticles. Front Microbiol 7:1831. https://doi.org/10.3389/fmicb.2016.01831